Fabrication of Metallic Nanodot Arrays

Masahiko Yoshino and Motoki Terano

Contents

Abstract

Metal nanodot arrays exhibit unique optical characteristics, and they are expected to find widespread applications in biosensors and various optical devices. In this section, simple and efficient manufacturing processes are introduced for metal nanodot arrays. These processes are based on the combination of thin metal film coatings deposited on substrates and thermal dewetting. The first process discussed herein is a conventional thermal dewetting method. With this method, it is shown that the average dot diameter can be controlled based on the chosen

M. Yoshino (✉)
Department of Mechanical Engineering, Tokyo Institute of Technology, Tokyo, Japan
e-mail: myoshino@mes.titech.ac.jp

M. Terano
Department of Mechanical Systems Engineering, Okayama University of Science, Okayama, Japan
e-mail: m_terano@mech.ous.ac.jp

process conditions. The second process is based on the use of grid patterning on coated metal films. This process can allow fabrication of nanodot arrays with uniform dot diameters and achieve highly ordered alignment of dots. The third process generates a metal nanodot array based on a self-organization manner on a nanogrid-patterned substrate. It constitutes a high-productivity process based on the transfer of the metal nanodot array to an adhesive film. The basic mechanisms underlying these processes are discussed herein.

1   Introduction

It is known that a collective oscillation of free electrons is induced in a metal surface when visible or infrared light is projected to this surface, whereby light of a specific wavelength is strongly absorbed or reflected. This phenomenon is called surface plasmon resonance (SPR). Since SPR is very sensitive to surface conditions, such as molecular adsorption to metal surfaces, it is used in various optical devices, including biosensors. However, SPR occurs only when the incident light and the metal surface are arranged in specific geometric positions, and a precise apparatus design is necessary to use SPR for biosensors.

While SPR occurs on the metal surface, localized surface plasmon resonance (LSPR) occurs on the surface of metal nanoparticles (Mortazavi et al. 2012). When light is projected to metal nanoparticles, the collective oscillation of free electrons induces polarization in the nanoparticles, and plasmons are localized on the surface. LSPR depends on the refractive index of the medium around the metal nanoparticles. Plasmonic sensors utilizing this phenomenon have been studied previously (Hong et al. 2012; Raphael et al. 2012; Sepulveda et al. 2009; Kajiura et al. 2009). Furthermore, a strong electric field is generated in the vicinity of the surface of the nanoparticles owing to the occurrence of LSPR, and a particularly strong electric field is induced in the narrow gap between adjacent nanoparticles. This phenomenon is useful for increasing the sensitivity of Raman spectroscopy. In this way, application of fine metal particles to various sensor devices is expected.

In the case of Au nanoparticles or Ag nanoparticles, LSPR is induced by visible light or infrared light. Since infrared light often interact with molecules, LSPR can be combined with spectroscopic analyses of fluorescence, or Raman scattering. Thus, applications of gold or silver nanoparticles have been attracting increasing attention (Zeng et al. 2011). Many applications are expected for these nanoparticles owing to these optical properties that can control light behavior at the nanoscale, and they are envisaged to serve an important role in combination with photonics and electronics. For example, studies on plasmonic biosensors (Dmitriev et al. 2008; Saito et al.

2012; Otte et al. 2011), surface-enhanced Raman scattering (SERS) (Oh and Jeong 2012; Agapov et al. 2013), surface-enhanced fluorescence (SEF) (Zhang et al. 2012; Kandziolka et al. 2013), photodetector (Senanayake et al. 2011), applications to electromotive force devices (Tsai et al. 2010), etc. have already been reported.

These phenomena depend on the size and morphology of nanoparticles, and highly ordered nanoparticles exhibit higher performances than random ones. Since nanoparticles fixed on a solid material are easier to handle than powder or liquid solutions of nanoparticles, uniform nanoparticles aligned on a substrate with a regulated layout are useful. We refer to these ordered metal nanoparticles that are aligned on a transparent substrate as metal nanodot array.

To allow the translation of the metal nanoparticles to these practical applications, it is necessary to develop an efficient fabrication process for metal nanoparticles. Various nanofabrication techniques have been studied to produce metal nanodot arrays with reproducible and controllable morphologies.

Such metallic nanostructures can be implemented using conventional lithographic methods, such as the ultraviolet lithography process (UVL) or the electron beam lithography process (EBL). Although these processes are advantageous for mass production of complex and fine nanostructures, like integrated circuits in semiconductors, large and expensive facilities are needed in which stringent process control is required. Additionally, focused ion beam (FIB) systems are utilized for machining various nano-sized structures in many laboratories since they can etch various materials with an ion beam according to computer-controlled patterns. However, this technology is not suitable for mass production of nanostructured devices because of its low-machining rates and high facility costs.

Nanoimprint lithography (NIL) was developed as an efficient method for nano-patterning (Chou et al. 1996; Lucas et al. 2008). The lithographic processes, such as resist coating, etching, and lift-off processes, are used in the same way as in conventional lithographic methods. No-resist nanoimprinting in metal was also reported to fabricate plasmonic nanostructures with high resolution and low cost (Varghese et al. 2013). However, the nanostructure mold used in the NIL process was made based on EBL and etching processes. Hence, NIL depends on conventional lithographic procedures.

Meanwhile, in order to reduce the facility cost and increase productivity, self-organization processes are attracting increasing attention. To this date, researchers have developed nanosphere lithography (Knoben et al. 2011; Cheung et al. 2006) and porous anodic alumina (PAA) (Saito et al. 2012; Huang et al. 2010). These methods are able to fabricate periodic metal dot patterns on a substrate using comparably simple experimental procedures and do not need accurate control of equipment. However, they have limitations in terms of the geometric specifications of the constructed nanostructures. Another process for high-throughput and low-cost fabrication of a metal nanodot array is the thermal dewetting method (Tan et al. 2012; Agapov et al. 2013; Lee et al. 2009; Leem et al. 2012). This process consists of spatter coating and thermal dewetting subprocesses and is much simpler than other nanofabrication processes. However, it also has limitations in terms of controlling the size and morphology of nanodots.

The authors have been developing a high-throughput fabrication process of metal nanodot arrays in which Au or Ag particles with several hundred nanometers in diameter are regularly arranged on a substrate, such as glass (Yoshino et al. 2011; Yoshino et al. 2012). In order to address problems of conventional processes, the authors employed combinations of precision machining and self-organization methods. Three self-organization processes of nanodot arrays are introduced in this chapter.

2 Fabrication Process of a Metal Nanodot Array by Thermal Dewetting

2.1 Experimental Studies

Figure 1 illustrates a conventional self-organization process of a metal nanodot array by means of the thermal dewetting method. In this process, a substrate is cleaned in an ultrasonic acetone bath and then dried. The substrate should be constructed using a high-melting-point material, and the interface energy between the metal of the nanodots and the substrate should be moderately low. A metal film is deposited on a substrate by using a spatter coater. The coated substrate is then annealed in an electric furnace. Based on the thermal dewetting mechanism, the coated metal film is separated into many small pieces and agglomerated into small semispherical dots. As a result, many random metal nanodots are generated on the substrate.

Figure 2 shows field emission scanning electron microscope (FE-SEM) micrographs of Au nanodots generated using this process on various types of substrates, i.e., (a) quartz glass, (b) single crystal quartz, (c) (1 0 0) silicon wafer, and (d) sapphire wafer. In this experiment, an Au thin film was deposited on these substrates in argon gas atmosphere using a direct current (DC) sputter coater. The pressure was 10 Pa, the ionization current was 5 mA, the distance between the substrate and the target was 35 mm, and the spattering time was adjusted so that the thickness of the Au thin film was 10 nm. These coated specimens were then inserted into an electric furnace preheated to annealing temperatures (700 °C.). After they were annealed in the furnace for 10 min, the substrates were taken out from the
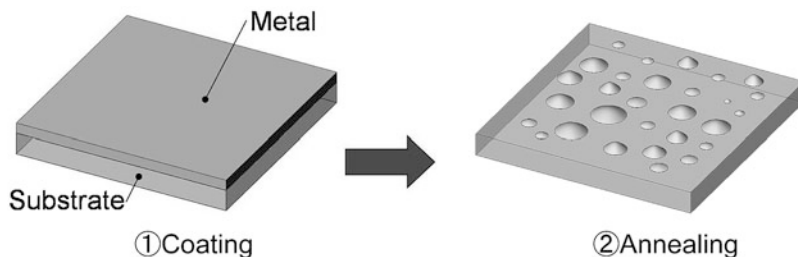
Fig. 1 Schematic illustration of the examined processes for nanodot array fabrication
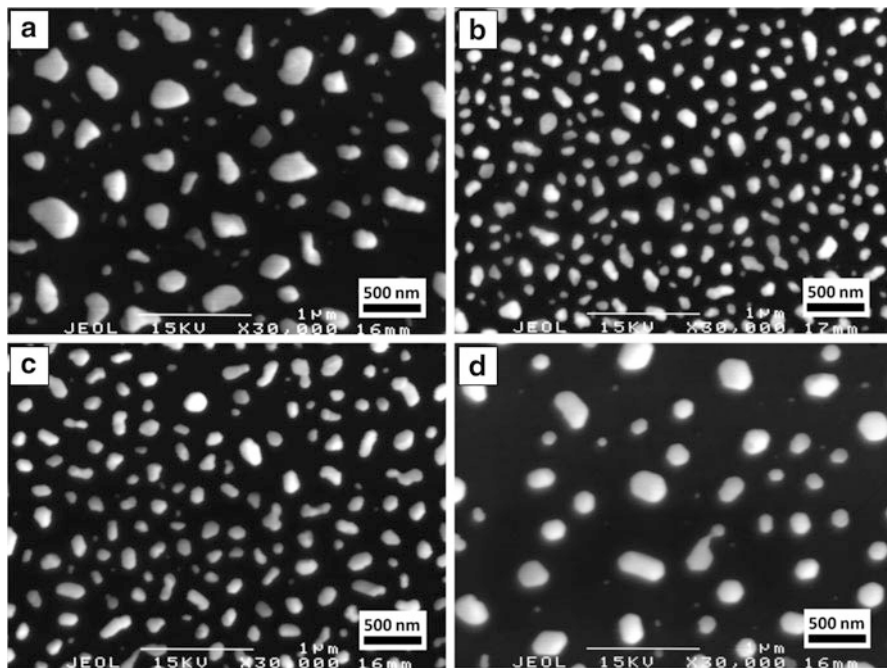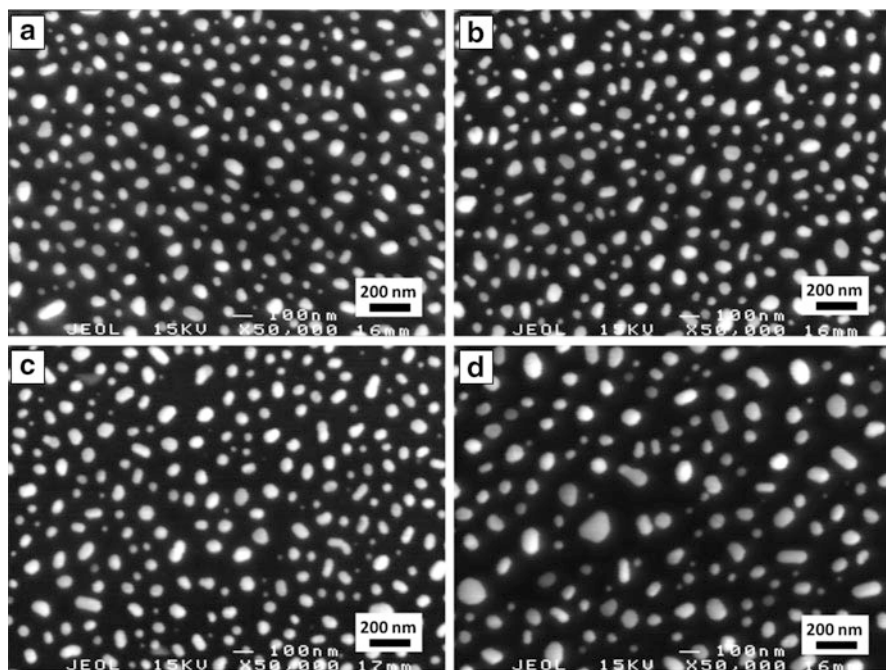
Fig. 2 Au nanodots generated on various substrates using the thermal dewetting method: (**a**) quartz glass plate, (**b**) quartz wafer, (**c**) silicon wafer, and (**d**) sapphire wafer. Annealing condition: 700 °C × 10 min

furnace and cooled down in air. Although annealing was conducted in air atmosphere, the effect of the oxidization on Au film and substrates was negligible.

These results indicate that the size and arrangements of generated dots are random, but the dot size depends on the material of the substrate. It is apparent that the dot sizes on (a) the quartz glass substrate and on (d) the sapphire wafer substrate are large, whereas the corresponding sizes on (b) the single crystal quartz substrate and on (c) the silicon wafer substrate are relatively small.

Figure 3 shows results of similar experiments using a platinum (Pt) film on these substrates. The thickness of the Pt thin film was 10 nm, and the annealing condition was 900 °C for 10 min in atmospheric air. Similar to the Au dots in Fig. 2, the sizes and arrangement of generated dots are random. Dots in Fig. 3 are apparently smaller than those in Fig. 2.

Figure 4a compares the average dot diameter (column) and the standard deviation (error bar) of Au nanodots and Pt nanodots observed in Figs. 2 and 3. Apparently, the average diameter and the standard deviation of Au nanodots are larger than those of the Pt nanodots. In addition, it is found that the influence of the substrate material on the average dot diameter is significant for Au nanodots, but it is less pronounced for Pt nanodots. Figure 4b compares the relative standard deviations of dot diameters. The standard deviation of Au nanodots on the quartz glass substrate exceeds 50%,

Fig. 3 Pt nanodots generated on various substrates using the thermal dewetting method: (**a**) quartz glass plate, (**b**) quartz wafer, (**c**) silicon wafer, and (**d**) sapphire wafer. Annealing condition: 900 °C × 10 min

and these dots are fairly larger than those on the quartz and silicon substrates. Meanwhile, the relative standard deviation of Pt nanodots is approximately 30% for all tested substrates. These characteristics are attributed to interface energy differences between the metal film and the substrate.

Figure 5 shows the change of morphology of agglomerating Au nanodots as a function of annealing temperature in the in situ SEM observation of annealing. In this experiment, thin Au films were coated on quartz glass substrates with a thickness of 10 nm. These substrates were then annealed in the SEM. Temperature was increased gradually to 700 °C, and change of morphology was observed continuously. When the temperature became (a) 550 °C, voids and pileups appear on the coated film. When the temperature became 600 °C, voids connected each other, due to growth of the voids, and the coated film was separated into many pieces of complicated island shapes, as indicated in Fig. 5b. When the temperature became 650 °C, these pieces were further separated into smaller particles (Fig. 5c). When the temperature reached 700 °C, these particles were agglomerated into round dots, as indicated in Fig. 5d.

These experimental results confirmed that the thermal dewetting process depends on the combination of substrate material, metal, and annealing time. Although

Fig. 4 Comparison of (**a**) the average dot diameter (column) and the standard deviation (error bar) of the Au nanodots and Pt nanodots and (**b**) the relative standard deviations estimated from Figs. 2 and 3
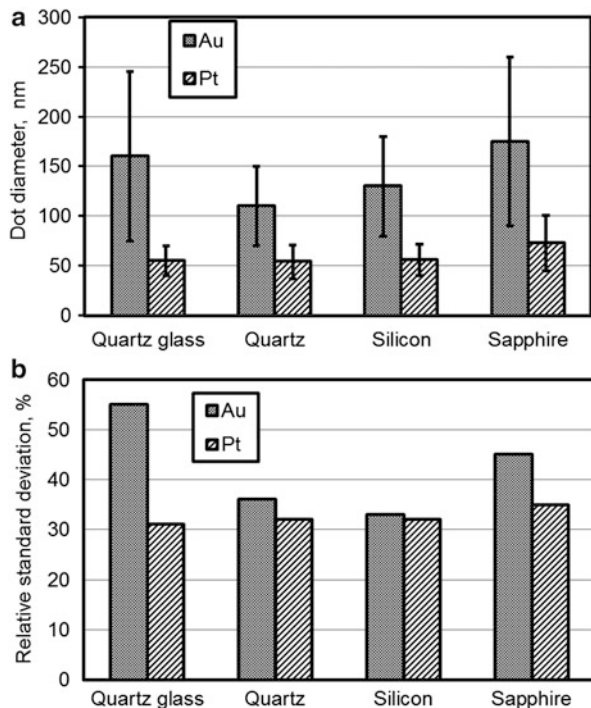

experimental data are not shown herein, it was also confirmed that the film thickness and annealing temperature also influenced the thermal dewetting process.

2.2 Theoretical Study of the Thermal Dewetting Mechanism

Many researchers have studied mathematical models describing the thermal dewetting of a metal film coated on a substrate in order to reveal the effects of the processing conditions on thermal dewetting (Cheynis et al. 2011; Danielson et al. 2006; Rayleigh 1879). However, to this date, the effects exerted by the surface energies and the contact angle between the metal layer and substrate on the size of the subsequently formed dots have not been clarified.

The authors considered a mathematical model of thermal dewetting where a deposited metal film agglomerated into a hemispherical metal dot (Yoshino et al. 2015). Figure 6 illustrates the assumed thermal dewetting process. Firstly, a metal film is deposited on the surface of a substrate with a high melting temperature, such as silicon wafer or quartz glass. The specimen is then annealed in a furnace at a lower temperature compared to the melting temperature of the metal film, and metal atoms migrate to stable positions based on diffusion. (1) Defects existing in the deposited metal film (Zhigal'skii and Jones 2003) are widened to form voids based on diffusion, and many voids appear on the metal film at the beginning of the thermal
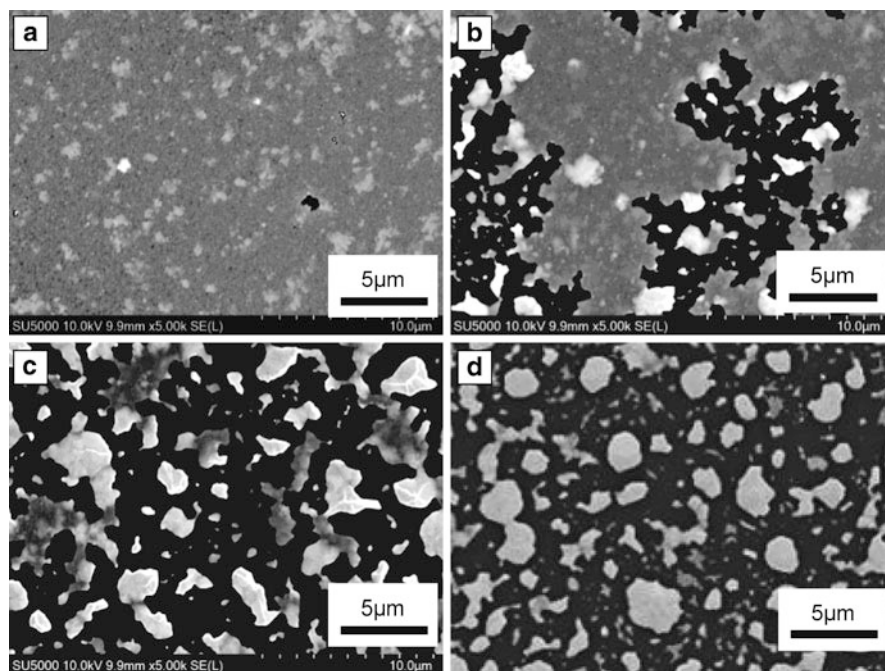
Fig. 5 Change of morphology of Au nanodots as a function of the annealing temperature in the in situ SEM observation of annealing: (**a**) 550 °C, (**b**) 600 °C, (**c**) 650 °C, and (**d**) 700 °C, when the annealing temperature was increased gradually

dewetting process. (2) As the voids grow, they start to become connected to adjacent voids. (3) These voids separate the metal film into many islands. (4) Each isolated metal island agglomerates into a hemispherical dot. Throughout this process, the free energy of the metal and substrate system is reduced.

We consider herein a simplified model of this thermal dewetting process where a plane metal film agglomerates into a hemispherical dot, as shown in Fig. 7. This constitutes an axisymmetric model around the centerline of the dot, where D_0 is the average diameter of a circular substrate that agglomerates into a single hemispherical dot. In this model, the dot shape is maintained hemispherical throughout the agglomeration process, D is the temporal dot diameter during agglomeration, and D_c is the final dot diameter at the stable state. The dot's height gradually increases as the dewetting time increases, when the angle θ between the dot surface and the substrate at the dot's periphery also increases. Hereafter, θ is referred to as the temporal contact angle. The temporal contact angle θ corresponds to the contact angle θ_c at the end of the agglomeration when the dot attains a stable state. It is known that the contact angle θ_c is related to the surface energies based on Young's equation (Young 1805):
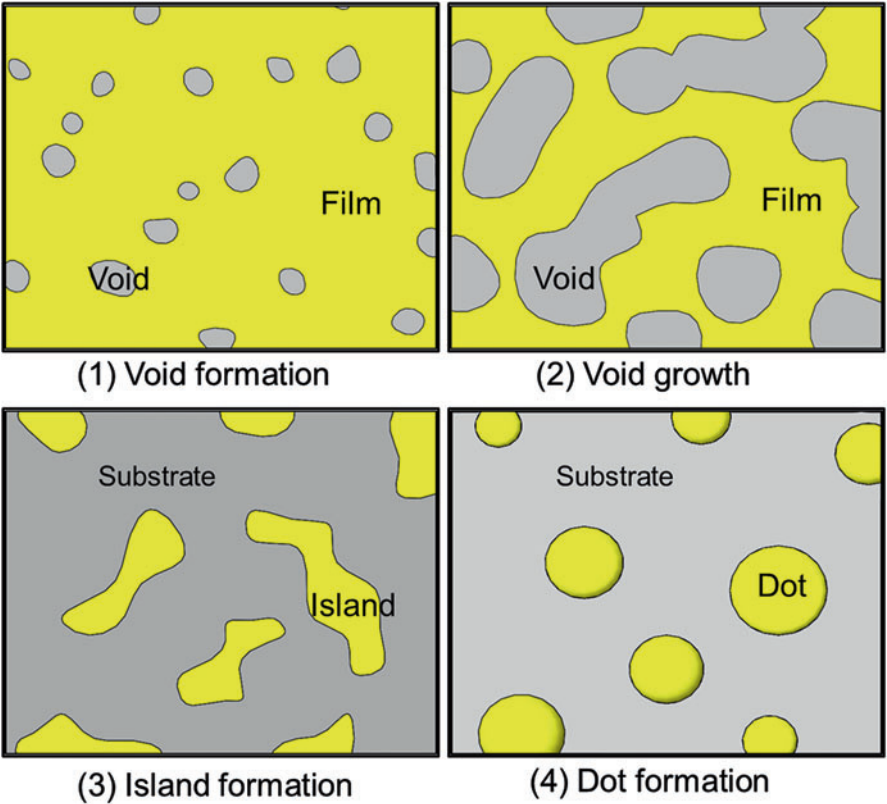
Fig. 6 Thermal dewetting process of a metal film deposited on a substrate

Fig. 7 Geometrical model of a metal and substrate system during the agglomeration
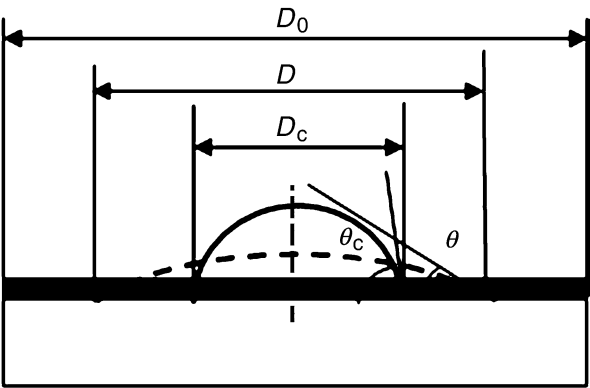
$$\gamma_I - \gamma_S = -\gamma_M \cos\theta_c \tag{1}$$

where γ_M is the surface energy per unit area of the metal, γ_s is that of the substrate, and γ_I is the interfacial energy between the metal and the substrate.

Using these energies, the total free energy of the substrate and metal system before annealing G_1 can be calculated by,

$$G_1 = A\gamma_M + A\gamma_I = A(\gamma_M + \gamma_I) \tag{2}$$

where A is the area of the substrate and is calculated by

$$A = \pi\,D_0{}^2/4 \tag{3}$$

Substituting Eq. 3 into Eq. 2, we obtain

$$G_1 = \frac{\pi\,D_0{}^2}{4}(\gamma_M + \gamma_I) \tag{4}$$

Since the total free energy of the system G_2 during agglomeration is the sum of the surface energy of a dot, the surface energy of the exposed substrate and the interfacial energy G_2 is calculated by

$$G_2 = S_M\gamma_M + S_I\gamma_I + (A - S_I)\gamma_S \tag{5}$$

where S_M is the area of the surface of the hemispherical metal dot and S_I is the area of interface between the metal dot and substrate.

When the temporal contact angle θ is smaller than 90°, S_M and S_I are calculated by

$$S_M = \frac{\pi D^2}{2}\frac{1 - \cos\theta}{\sin^2\theta} \tag{6}$$

$$S_I = \frac{\pi D^2}{4} \tag{7}$$

Using Eqs. 5, 6, and 7, and Young's Eq. 1, we obtain

$$G_2 = \frac{\pi D^2}{4}\frac{\gamma_M}{1 + \cos\theta}\{2 - (1 + \cos\theta)\cos\theta_c\} + \frac{\pi D_0{}^2}{4}\gamma_S \tag{8}$$

Thus, reduction of the total free energy by agglomeration is obtained as

$$\Delta G = G_1 - G_2 = \frac{\pi\,\gamma_M}{4}\left\{D_0{}^2(1 - \cos\theta_c) - D^2\frac{2 - \cos\theta_c - \cos\theta\cos\theta_c}{1 + \cos\theta}\right\} \tag{9}$$

When the temporal contact angle θ is greater than 90°, S_M and S_I are calculated by

$$S_M = \frac{\pi D^2}{2}(1 - \cos\theta) \tag{10}$$

$$S_I = \frac{\pi D^2}{4}\sin^2\theta \tag{11}$$

Using Eqs. 5, 10, and 11, and the Young's Eq. 1, we obtain

$$G_2 = \frac{\pi\ D^2}{4}\gamma_M\{2 - 2\cos\theta - \sin^2\theta\cos\theta_c\} + \frac{\pi\ D_0^2}{4}\gamma_S \tag{12}$$

In this case, reduction of the total free energy by agglomeration is

$$\Delta G = G_1 - G_2$$
$$= \frac{\pi\ \gamma_M}{4}\{D_0^2(1 - \cos\theta_c) - D^2(2 - \cos\theta - \sin^2\theta\cos\theta_c)\} \tag{13}$$

Herein, we define the nondimensional energies of G_1, G_2, and ΔG as follows:

$$\Gamma_1 = \frac{G_1}{t^2\gamma_M} = \frac{\pi}{4}\xi_0^2\left(1 + \frac{\gamma_I}{\gamma_M}\right) \tag{14}$$

$$\Gamma_2 = \frac{G_2}{t^2\gamma_M} = \frac{\pi\ \Xi_0^2}{4}\left\{\frac{2 - \cos\theta_c - \cos\theta\cos\theta_c}{1 + \cos\theta}\frac{\xi^2}{\Xi_0^2} + \frac{\gamma_S}{\gamma_M}\right\} \quad \theta < 90° \tag{15}$$

$$\Gamma_2 = \frac{G_2}{t^2\gamma_M} = \frac{\pi\ \Xi_0^2}{4}\left\{(2 - 2\cos\theta - \sin^2\theta\cos\theta_c)\frac{\xi^2}{\Xi_0^2} + \frac{\gamma_S}{\gamma_M}\right\} \quad \theta > 90° \tag{16}$$

$$\Delta\Gamma = \frac{\Delta G}{t^2\gamma_M} = \frac{\pi}{4}\Xi_0^2\left\{(1 - \cos\theta_c) - \frac{\xi^2}{\Xi_0^2}\frac{2 - \cos\theta_c - \cos\theta\cos\theta_c}{1 + \cos\theta}\right\} \quad \theta < 90° \tag{17}$$

$$\Delta\Gamma = \frac{\Delta G}{t^2\gamma_M} = \frac{\pi}{4}\Xi_0^2\left\{(1 - \cos\theta_c) - \frac{\xi^2}{\Xi_0^2}(2 - \cos\theta - \sin^2\theta\cos\theta_c)\right\} \quad \theta > 90° \tag{18}$$

where ξ and ξ_0 are normalized diameters defined by

$$\xi = \frac{D}{t} \tag{19}$$

$$\Xi_0 = \frac{D_0}{t} \tag{20}$$

2.3   Minimum Nanodot Size

It is also assumed that the metal volume is conserved throughout a dewetting process because the annealing temperature is much lower than the melting temperature of the deposited metal. When the temporal contact angle θ is smaller than 90°, the volume of a hemispherical dot V is calculated as

$$V = \frac{\pi}{24} \frac{D^3}{\sin^3\theta} \left(2 - 3\cos\theta + \cos^3\theta\right) \tag{21}$$

Because the volume of a dot is equivalent to the volume of a metal film deposited on the substrate, the following equation is obtained:

$$V = \frac{\pi}{24} \frac{D^3}{\sin^3\theta} \left(2 - 3\cos\theta + \cos^3\theta\right) = At = \frac{\pi}{4} D_0^2 t \tag{22}$$

Thus, the dot diameter is calculated as

$$D = \left(\frac{6\sin^3\theta \; D_0^2 t}{2 - 3\cos\theta + \cos^3\theta}\right)^{1/3} \tag{23}$$

This is rewritten as follows using the nondimensional diameters,

$$\xi = \frac{D}{t} = \left(\frac{6 \; \Xi_0^2}{2 - 3\cos\theta + \cos^3\theta}\right)^{1/3} \sin\theta \tag{24}$$

When the temporal contact angle θ is greater than 90°, we obtain

$$\xi = \frac{D}{t} = \left(\frac{6\Xi_0^2}{2 - 3\cos\theta + \cos^3\theta}\right)^{1/3} \tag{25}$$

Figure 8 shows an example of calculated variations of Γ_1, Γ_2, and $\Delta\Gamma$ as a function of ξ using Eqs. 14, 18, 24, and 25. The parameters used in this calculation were

$$\theta_c = 90^\circ, \quad \gamma_M = 1, \quad \gamma_S = 1, \quad \gamma_I = 1, \quad \Xi_0$$
$$= 50, \quad \left(D_0 = 500\,\text{nm}, \quad A = 1.96 \times 10^5\,\text{nm}^2, \quad t = 10\,\text{nm}\right)$$

In this graph, agglomeration starts from $\xi = 50$ and finishes at $\xi = 20$. Γ_2 decreases when ξ decreases, and Γ_2 reaches its minimum value, and the contact angle attains θ_c when ξ becomes minimum. The final nondimensional dot diameter ξ_c is calculated by
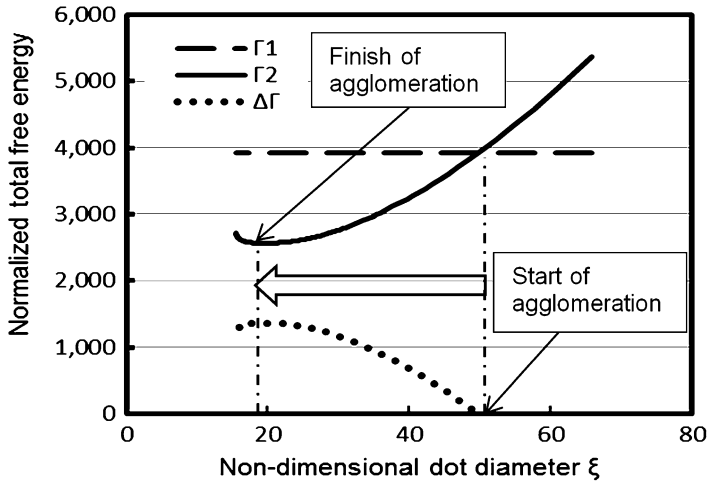
Fig. 8 Variation of the free energies as a function of the dot diameter ξ. Simulation parameters are $\theta_c = 90°$, $\gamma_M = 1$, $\gamma_S = 1$, $\gamma_I = 1$, $\xi_0 = 50$, ($D_0 = 500$ nm, $A = 1.96 \times 10^5$ nm^2, $t = 10$ nm)

$$\xi_c = \begin{cases} \left(\dfrac{6\ \Xi_0^2}{2 - 3\cos\theta_c + \cos^3\theta_c} \right)^{1/3} \sin\theta_c, & \text{when } \theta_c < 90° \\[3mm] \left(\dfrac{6\ \Xi_0^2}{2 - 3\cos\theta_c + \cos^3\theta_c} \right)^{1/3}, & \text{when } \theta_c \geq 90° \end{cases} \tag{26}$$

In addition, Eqs. 17 and 18 indicate that $\Delta\Gamma$ depends on Ξ_0 and that the driving force of agglomeration is weakened when ξ_0 becomes smaller. Because $\Delta\Gamma$ must be positive to initiate the dot agglomeration process,

$$\Delta\Gamma = \frac{\pi}{4}\Xi_0^2 \left\{ (1 - \cos\theta_c) - \frac{\xi^2}{\Xi_0^2} \frac{2 - \cos\theta_c - \cos\theta\cos\theta_c}{1 + \cos\theta} \right\} > 0 \quad \theta < 90° \tag{27}$$

$$\Delta\Gamma = \frac{\pi}{4}\Xi_0^2 \left\{ (1 - \cos\theta_c) - \frac{\xi^2}{\Xi_0^2} \left(2 - \cos\theta - \sin^2\theta\cos\theta_c \right) \right\} > 0 \quad \theta > 90° \tag{28}$$

By substituting Eqs. 24 and 25, the minimum substrate diameter Ξ_{0min} is determined as

$$\Xi_{0min} = 6\sqrt{\frac{2 + \cos\theta_c}{1 - \cos\theta_c}} \quad \left(\text{for } \theta < 90° \text{ and } \theta > 90° \right) \tag{29}$$

If the diameter of the substrate per dot is smaller than Ξ_{0min}, the metal film cannot become a hemispherical dot but remains as a metal film on the substrate. Thus, the minimum dot diameter ξ_{min} generated from the minimum substrate diameter Ξ_{0min} is obtained as follows:

Fig. 9 The relationship
between the dot diameter and
the contact angle
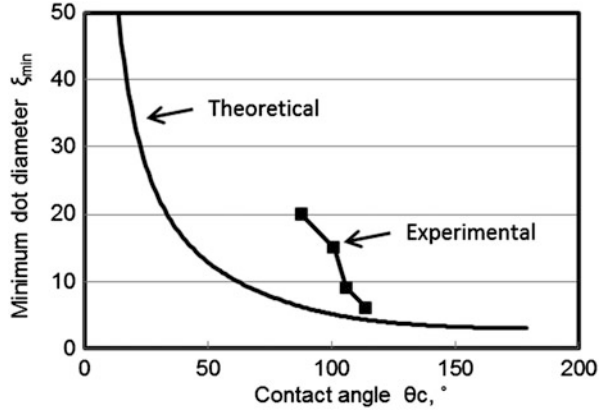
$$\xi_{\min} = \begin{cases} \dfrac{6 \sin \theta_c}{1 - \cos \theta_c} & \theta_c < 90^{\circ} \\ \dfrac{6}{1 - \cos \theta_c} & \theta_c > 90^{\circ} \end{cases} \tag{30}$$

The dot size generated by thermal dewetting cannot be smaller than the minimum dot diameter $\xi_{\min}$. Figure 9 shows the relationship between the dot diameter and the contact angle. The solid curve represents the variation of the minimum dot diameter $\xi_{\min}$. The solid symbols denote experimental data of the normalized average dot diameter of Au nanodots generated on substrates of various materials. It is found from this figure that both experimental and theoretical values elicit similar trends, whereby the dot diameter decreases as a function of the contact angle θ_c.

It is also found that the experimental dot diameter is larger than the theoretical dot diameter. This is because the dot diameter depends on the size of the islands that were separated by growing voids in the early stage of dewetting, as explained in Fig. 6. Since the number of the voids depends on the density of the initial defects in the deposited metal film, and the growth rate relies on the chosen annealing conditions, the dot diameter is influenced by the spattering and annealing conditions. The experimentally measured dot diameter will agree with the theoretically estimated dot diameter when the density of the initial defects in the deposited metal film is sufficiently high and annealing conditions are appropriate. Meanwhile, if there is no defect in the metal film, all of metal film aggregates into a dot. Correspondingly, very large metal dots are generated.

Accordingly, the average nanodot diameter depends on the contact angle, the defect density in the coated metal film, and the thickness of the coated film. Since the contact angle is dependent on the surface energies of the dot material and the substrate, it is not a controllable parameter when the combination of these materials is considered. The defect density in a coated metal depends on the spattering conditions, such as the spatter gas pressure, temperature of material, ionization voltage, and spattering current. Although these are controllable parameters, it is

difficult to control the defect density in the coated metal film by adjusting these parameters. However, the thickness of the coated film is easy to control accurately, and its effect on the average nanodot size is apparent. Additionally, the annealing condition is an effective parameter that controls the nanodot diameter. Once the materials of the nanodot and substrate are determined, the average nanodot size can be controlled by adjusting the spattering condition, thickness of the metal film, and the annealing condition.

3 Fabrication Process of a Metal Nanodot Array of Uniform Dot Size Based on the Combination of Nano-plastic Forming and Thermal Dewetting

3.1 Experimental Studies

As discussed in the previous section, the average nanodot size can be controlled by the thickness of the coated metal film in the conventional thermal dewetting process. However, the sizes of individual nanodots depend on the size of separated metal film islands, which in turn is attributed to the statistical distribution of defects in the metal film. Therefore, the dispersion of nanodot sizes cannot be controlled. In order to address this problem, the authors developed a new fabrication process of a metal nanodot array with a uniform dot size.

Figure 10 shows a new manufacturing process of a nanodot array. Firstly, the substrate is cleaned by ultrasound in an acetone bath, and a thin metal film is then deposited on the substrate using a sputter coater. A square nanogroove grid is then machined on the coated film using the nano-plastic forming (NPF) method. The details of NPF are explained below. Finally, the substrate is annealed in an electric furnace so that the thin metal film is aggregated into nanodots using the thermal dewetting mechanism.

In this section, experimental results are shown using quartz glass as the substrate. The thickness of the quartz glass substrate was a 1 mm, and its surface was finished by polishing. The quartz substrate was cleaned by ultrasound in an acetone bath and then dried. Thereafter, a thin Au film was deposited on the substrate using a DC sputter coater. The sputtering gas was Ar, and its pressure was 10 Pa. The thickness of the coated gold layer was set to 5 or 10 nm by controlling the sputtering time. After a square nanogroove grid was fabricated on the coated Au film using NPF, the substrate was annealed in an electric furnace in atmospheric air. The annealing temperature was 700 °C, and the annealing time was 10 min.

NPF is a metal-forming method applicable at the nano-/microscales. It can produce minute structures that are smaller than 1 μm only by indenting a specially designed tool directly on the work material. Figure 11 shows a NPF tester developed for the experiment. It consists of high-precision XY and Z stages. The feed resolution of the X stage is 1 nm, and those of the Y and Z stages are 10 nm. A specimen is set on the XY stage. A diamond tool and a load cell are mounted on the Z stage. The indentation load measured by the load cell is acquired by the computer and fed back
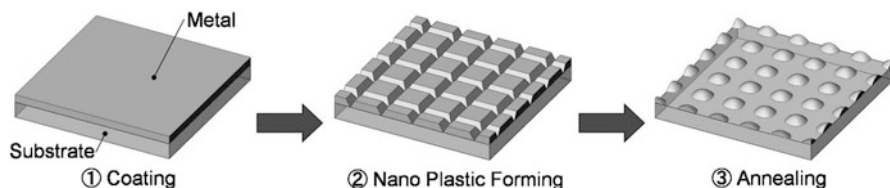
Fig. 10 Proposed fabrication process for the construction of a nanodot array

Fig. 11 Nano-plastic-forming tester
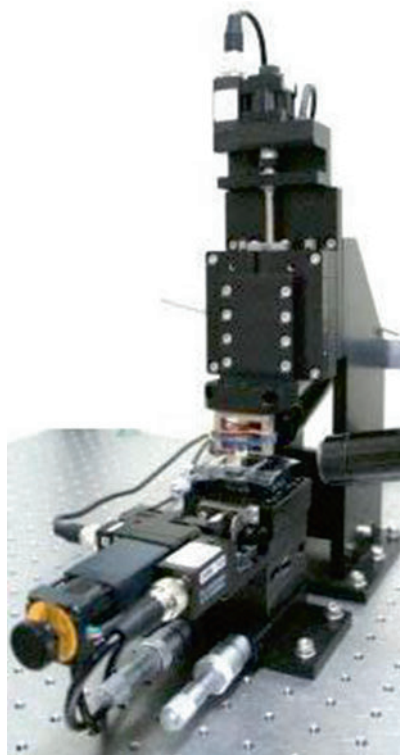
to control the motion of the Z stage to control the indentation load. The diamond tool is impressed on the specimen by moving the Z stage downward. All stage motions implemented during the NPF procedure are controlled by the computer. NPF is executed in a clean chamber so that the influence of dust is avoided.

Figure 12 shows an optical micrograph of a knife-edge tool used by the NPF for nanogroove grid patterning. It is made of a single crystal diamond. Its length is 1 mm, and its edge angle is 60°. Its ground edge was very sharp, and the edge radius was smaller than 50 nm.

Figure 13 shows an SEM image of a nanogroove grid formed on the gold thin film coated on the quartz glass substrate. This image is an example of a groove grid with a
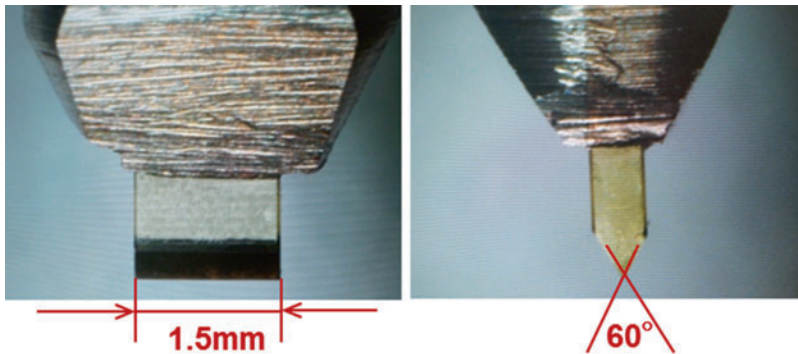
**Fig. 12** Knife-edge tool used for nanogroove grid patterning using NPF

Fig. 13 FE-SEM micrographs of nanogroove grids on the coated gold layer. The thickness of the gold film is 10 nm, and the indentation load is 0.5 N
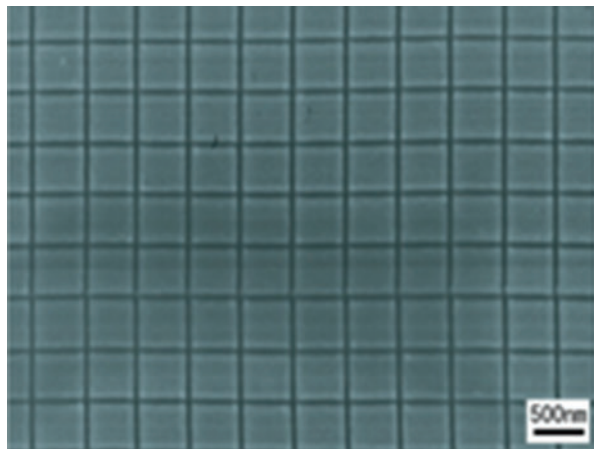
500 nm interval. The thickness of the gold film was 10 nm. The indentation load was 0.5 N. It is confirmed that very thin grooves can be fabricated by simple indentation of the knife-edge tool. In spite of the plastic deformation of the gold layer induced by NPF, the gold layer was maintained attached on the substrate.

Figure 14 shows the nanodot arrays generated on the quartz glass substrate based on annealing. Metal films were agglomerated into small dots by the thermal dewetting mechanism.

Dots are approximately located at the centers of each of the grid squares except in (a). In Fig. 5a, the thickness of the coated film and grid size of (a) were 10 and 1000 nm, respectively. The Au film was separated into several dots in each grid and was agglomerated into random nanodots. The average diameter of the agglomerated nanodots was 235 nm with a relative standard deviation of 22%. In contrast, in Fig. 5b, the thickness of the coated film and grid size were, respectively, equal to 10 and 500 nm, and a dot was agglomerated at the center of each grid. The dot size was almost uniform, and dots were aligned in a regular grid pattern. The average
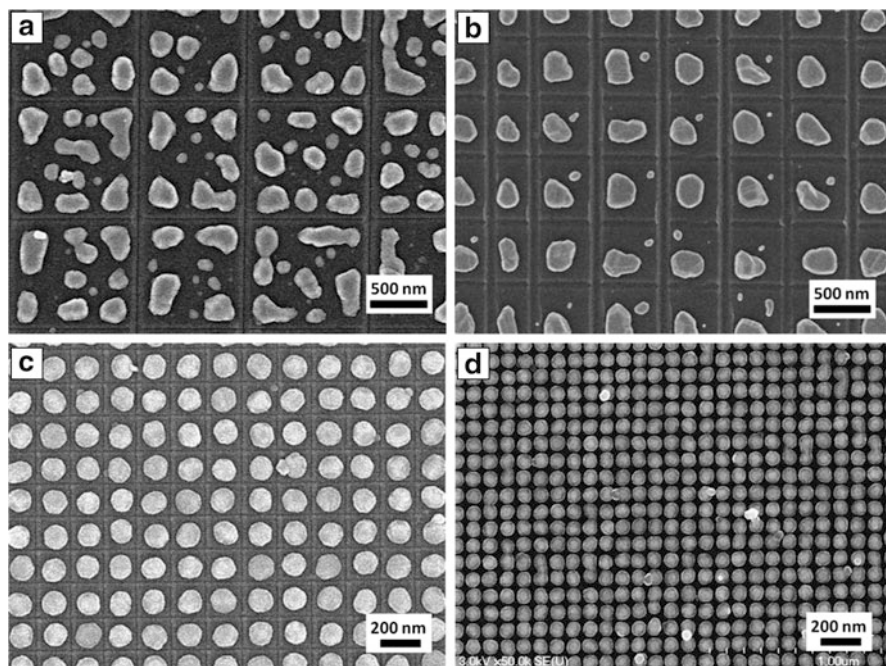
Fig. 14 FE-SEM micrographs of Au nanodot arrays. The thicknesses of the metal films and the grid sizes were (**a**) 10 nm and 1000 nm, (**b**) 10 nm and 500 nm, (**c**) 5 nm and 175 nm, and (**d**) 5 nm and 100 nm. Annealing conditions were 700 °C × 10 min

diameter of the nanodots was 187 nm with a relative standard deviation of 7%. In Fig. 5c, the thickness of the coated film was 5 nm, and the grid size was 175 nm. The Au nanodots were aligned in a regular grid pattern, and the dot sizes were uniform. The average diameter of the nanodots was 125 nm, and the standard deviation was 2%. Additionally, in Fig. 5d, when the thickness of the coated film was 5 nm and the grid size was 100 nm, many dots were aligned in the grid pattern. The average diameter of the nanodots was 93 nm, and the standard deviation was 2%.

Figure 15 shows an FE-SEM micrograph of the Au nanodot array where the thickness of the metal film is 5 nm and the grid size is 75 nm. It is found that many dots were aligned within the grid pattern, but many dots were bonded with neighboring dots. The average diameter of the nanodots was 79 nm, but the standard deviation was 19%, values that are fairly larger than those corresponding to the results of Fig. 14.

These results indicate that the size and distance of the nanodots are determined by the size of the groove grids. Since the metal film is separated into uniform square shapes using NPF, dots are agglomerated in a regular lattice pattern with uniform dot distances, as seen in Fig. 14b–d. However, when the grid size is too large, as shown in Fig. 14a, the metal films in each grid was separated into multiple dots. This is because the grid size was larger than the minimum dot diameter. In contrast, when

Fig. 15 FE-SEM micrographs of the Au nanodot array, whereby the thickness of the metal film is 5 nm and the grid size is 75 nm. The annealing conditions were 700 °C × 10 min
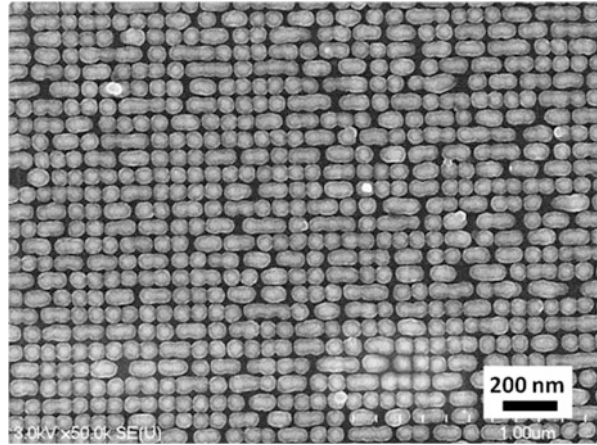
the grid size is too small, as seen in Fig. 15, dots are not separated by the groove grids because the grid size was smaller than the minimum dot diameter. These problems can be solved by controlling the thickness of the coated metal film. It has also been confirmed that nanodot arrays with arbitrary sizes in the range of several tens to several hundreds of nm can be fabricated using the proposed process.

Figure 16 shows the variation of the average diameter of nanodots (solid symbols), and their standard deviations (open symbols), as a function of grid size. Circles denote data of Au-coated films with 10 nm in thickness, while triangles denote corresponding data for films with 5 nm in thickness. The broken line indicates the limit of the nanodot's diameter that effectively equals the grid's size. It is confirmed from the figure that the average dot diameter increases when the grid size increases in instances when the grid size is smaller than 500 nm. However, the average diameter decreases when the grid size is 1000 nm. This is attributed to the separation of the dots within the grid squares, as shown in Fig. 14a. The relative standard deviation also decreases with decreases of the grid size. However, the relative standard deviation increases when the grid size becomes smaller than 100 nm. This is owing to the bonding of the nanodots, as observed in Fig. 15.

It should be noted that the relative standard deviations of these nanodots are much smaller than those of Fig. 4b, with the exception of the 1000 nm grid. This indicates that the uniformity of the dot size is much better than the conventional dewetting process. In addition, the layout of the nanodots is regulated very well, and the regularity of the dot alignment is apparently high. This new process is advantageous in terms of the uniformity and controllability of the dot's size and alignment.

3.2 Theoretical Study

Figure 17 illustrates the agglomeration process of nanodots by thermal dewetting. The coated metal film is separated into square grids by the groove grid. P is the
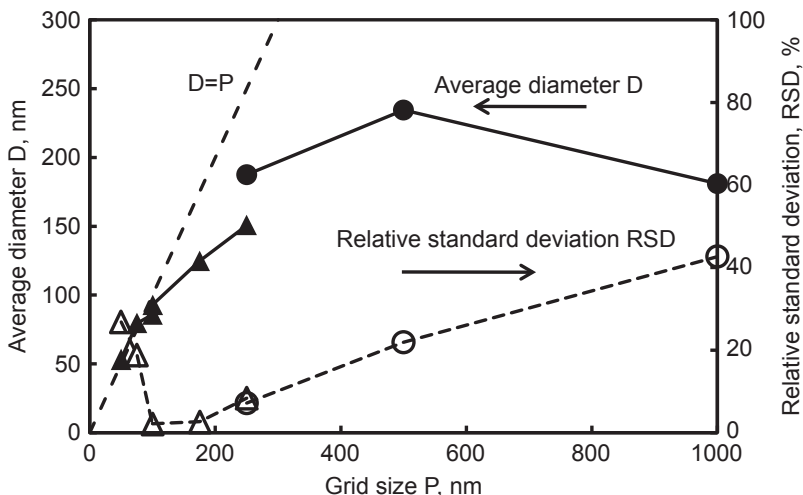
Fig. 16 Variation of the average nanodot sizes and relative standard deviations as a function of the grid size
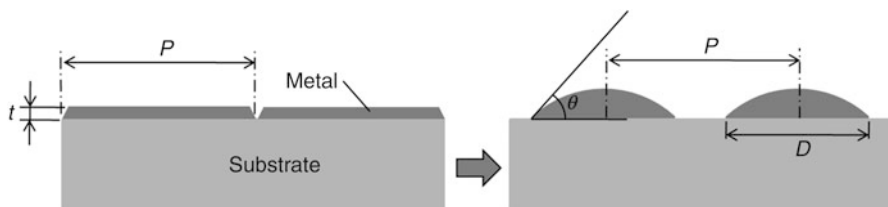

Fig. 17 Geometrical changes of nanodots incurred from the use of thermal dewetting

distance of grooves, which corresponds to the groove grid size. It is the thickness of the coated film. A coated metal film in each grid square agglomerates into hemispherical dots by thermal dewetting, as shown on the right subplot in Fig. 17. In this case, D is the diameter of the dot, and θ_c is the contact angle of a nanodot. By assuming that the volume conservation of the metal film occurs throughout the thermal dewetting process, the following equations are obtained:

$$D = \left\{ \frac{24P^2 t \sin^3 \theta_c}{\pi(2 - 3\cos\theta_c + \cos^3\theta_c)} \right\}^{\frac{1}{3}} \quad (0° < \theta_c \leq 90°) \tag{31}$$

$$D = \left\{ \frac{24P^2 t}{\pi(2 - 3\cos\theta_c + \cos^3\theta_c)} \right\}^{\frac{1}{3}} \quad (90° \leq \theta_c \leq 180°) \tag{32}$$
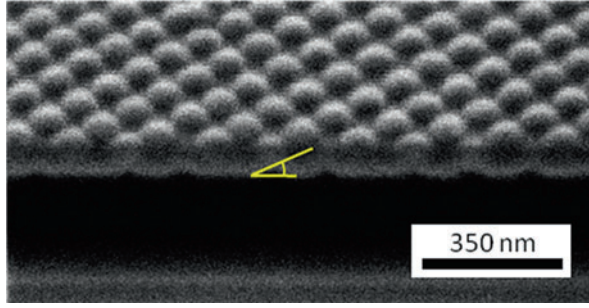
Fig. 18 Scanning ion microscopy (SIM) image of a cross section of a nanodot array. The thickness of the gold layer was 5 nm, patterned grid size was 100 nm, annealing temperature was 700 °C, and the annealing time was 10 min. The cross section was machined by an FIB and was observed at an angle of 45° defined in an anticlockwise direction with respect to the specimen's surface

The contact angle was measured from the cross section of nanodots in Fig. 18. Figure 18 shows a scanning ion microscopy (SIM) image of a cross section of a nanodot array, where dots were sectioned by FIB etching. In the figure, the cross section was observed obliquely at an angle of 45° defined in an anticlockwise direction with respect to the substrate's surface. By compensating the inclined angle of observation, we estimated that the contact angle was almost 41°.

Figure 19 shows the relationship between the nanodot diameter D and the grid size P. Symbols denote the average diameter of the nanodots obtained by experiments where the thickness of the gold layer was 5 nm. The solid curve indicates the variation of the dot diameter of Eq. 3, where the contact angle θ is 41°. It is confirmed that the experimental data agree well with the theoretical values. The broken line represents the condition at which $D=P$, where dots are connected to neighboring dots. It is found from the figure that the solid line crosses the dashed line at $P = 64$ nm and exceeds the dashed line when the grid size is smaller than P_c. Therefore, 64 nm represents the minimum diameter of nanodots that can be fabricated under present condition.

Figure 20 shows the variation of the diameter of the nanodots calculated based on Eq. 31. Three levels of coating thicknesses are shown in the graph. The broken line indicates that $D=P$, and the cross point of the curve and dashed line indicate the minimum dot diameter. The minimum dot diameter equations are obtained from Eqs. 31 and 32 assuming validity of the condition whereby $D=P$.

$$D_{\min} = \frac{24t \sin^3\theta_c}{\pi \ (2 - 3\cos\theta_c + \cos^3\theta_c)} \quad (0° < \theta_c \leq 90°) \tag{33}$$

$$D_{\min} = \frac{24t}{\pi(2 - 3\cos\theta_c + \cos^3\theta_c)} \quad (90° \leq \theta_c \leq 180°) \tag{34}$$

Fig. 19 Relationship between the diameter of the nanodots and the grid size. Symbols are experimental data. The thickness of the gold layer was 5 nm. The solid curve is the theoretical value calculated using Eq. 3 where the contact angle is 41°
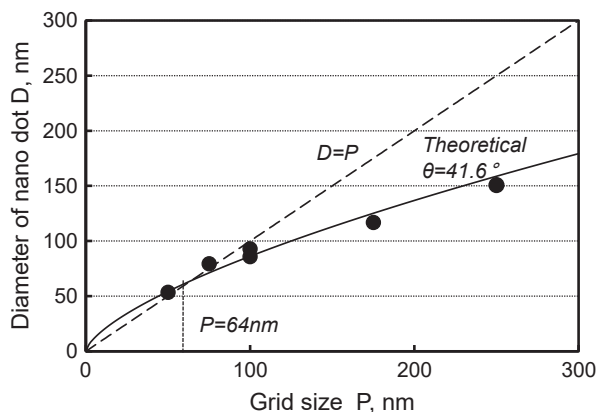
Fig. 20 Theoretical variation of the diameter of nanodots as a function of the grid size. The contact angle is 41°. The thicknesses of the gold layers are 1, 2, and 2.5 nm
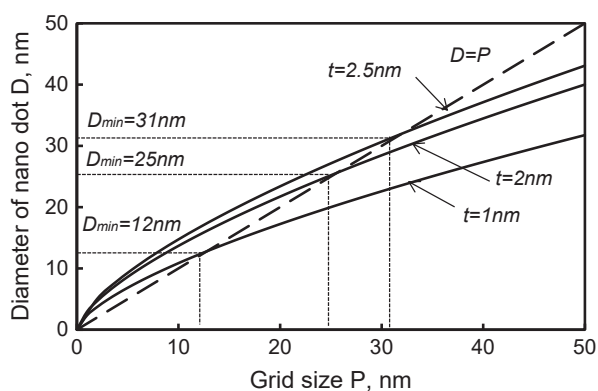
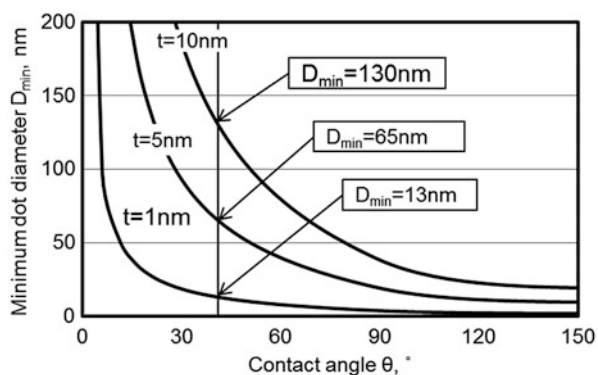**Fig. 21** Calculated variation of minimum diameter D_{min} against the contact angle θ

Figure 21 shows the calculated variation of the minimum dot diameter D_{min} as a function of the contact angle θ for three levels of the metal film thickness, i.e., 1, 5, and 10 nm. It is found that D_{min} decreases with the increase of the contact angle θ.

The vertical line in the graph indicates that $\theta = 41°$ and that the D_{min} values in the graph present the minimum dot diameter when $\theta = 41°$. The data of $D_{min} = 65$ nm on $t = 5$ nm agree with the experimental data shown in Fig. 19. This graph indicates that a very small nanodot array with a diameter of 13 nm can be fabricated when the coating thickness is 1 nm.

Accordingly, the dot diameter can be controlled by controlling the metal film thickness and the grid size, even when the combination of the substrate and nanodot material is determined.

4 Fabrication Process of a Metal Nanodot Array Using Patterned Substrates

4.1 Experimental Studies

Although the aforementioned method is effective for fabrication of metal nanodot arrays, there is a problem since a nanogroove grid has to be formed on each coated specimen. Since the NPF's operation time increases with the area of the nanodot array, this process is not suitable for mass production of large-area nanodot arrays. In order to overcome this disadvantage, authors are developing another manufacturing process for nanodot arrays (Truong et al. 2012).

Figure 22 illustrates the basic steps of this process. Specifically, a quartz glass plate on which a nanogroove grid was fabricated a priori is utilized as the substrate for the nanodot array. Subsequently, a thin Au film is coated on the substrate, and the substrate is annealed. The metal thin film naturally separates on the nanogrooves and self-organizes into a nanodot array. Thereafter, an adhesive polymer is pasted on the nanodot array and then peeled off. The nanodot array is transferred to the polymer film. This polymer film is used as a nanodot array. Since the substrate can be used repeatedly, the fabrication process of the nanogroove grid does not to be conducted for every nanodot array. Accordingly, high productivity can be achieved by the repetition of the Au film-coating process, self-organization using annealing, and transfer to polymer films.
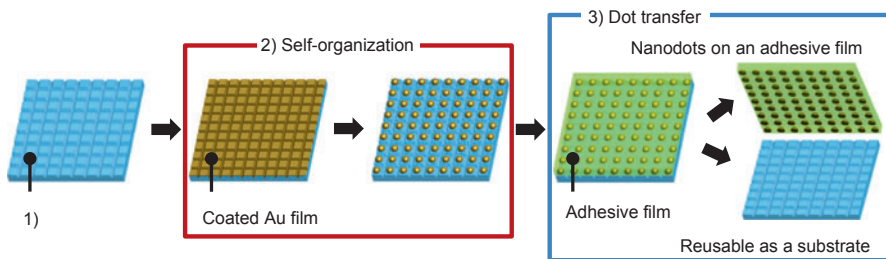
Fig. 22 Efficient fabrication process of nanodot arrays using a patterned substrate and dot transfer

Fig. 23 FE-SEM micrograph of a prepatterned quartz glass substrate coated with Au
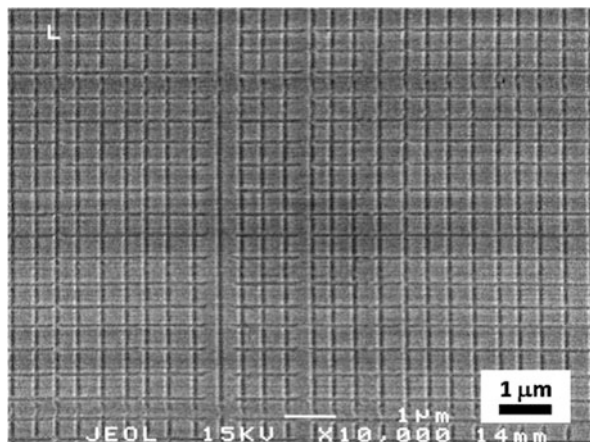

Figure 23 shows an FE-SEM micrograph of a quartz glass substrate on which a nanogroove grid of 500 nm square is fabricated using the EB lithographic method. The groove grid was fabricated on the substrate using the NPF method. The width and depth of the grooves were less than 100 nm. Many hard brittle materials, such as quartz glass, can be formed by plastic deformation without generating cracks when the depth of deformation is smaller than the critical depth. Since the critical depth of quartz glass is approximately 200 nm for a 60° knife-edge tool, nanogroove grids can be fabricated by nano-indentation of the knife-edge tool without generating cracks in the quartz substrate. In Fig. 23, although a thin Au film with a thickness of 10 nm is coated on the substrate, a nanogroove grid is observed.

Figure 24 shows FE-SEM images of nanodot arrays generated on the patterned substrates using annealing. The sizes of the groove grid that was preliminarily fabricated on the quartz glass substrate were (a) 250 nm, (b) 500 nm, and (c) 1000 nm. The thickness of the coated Au film was 10 nm, and the annealing condition was 700 °C × 10 min. In the case of (a) and (b), the Au nanodots are almost aligned in the center of each grid. Although the regularity is lower than that exhibited by the nanodots in the previous section, this is because the annealing conditions were not appropriate for this nanodot array. Small dots are found arranged in a lattice pattern between large nanodots. These are the Au dots that remained on the bottom of the groove grids of the quartz substrate. The Au thin film was separated on the grooves, and a separated film agglomerated into a large nanodot that was located at the center of the lattice. Most of the Au atoms were aggregated at the large nanodots based on diffusion, but some of the gold remained on the bottom of the groove, and formed small dots aligned along the grooves. In addition, plural dots were found in some of the grids. They were separated during the agglomeration process because the heat treatment conditions and spattering conditions were not appropriate for this grid size and film thickness. By adjusting these conditions, the separation of dots in a groove grid can be prevented. In (c), random and non-uniformly distributed dots were generated even though a groove grid was fabricated.
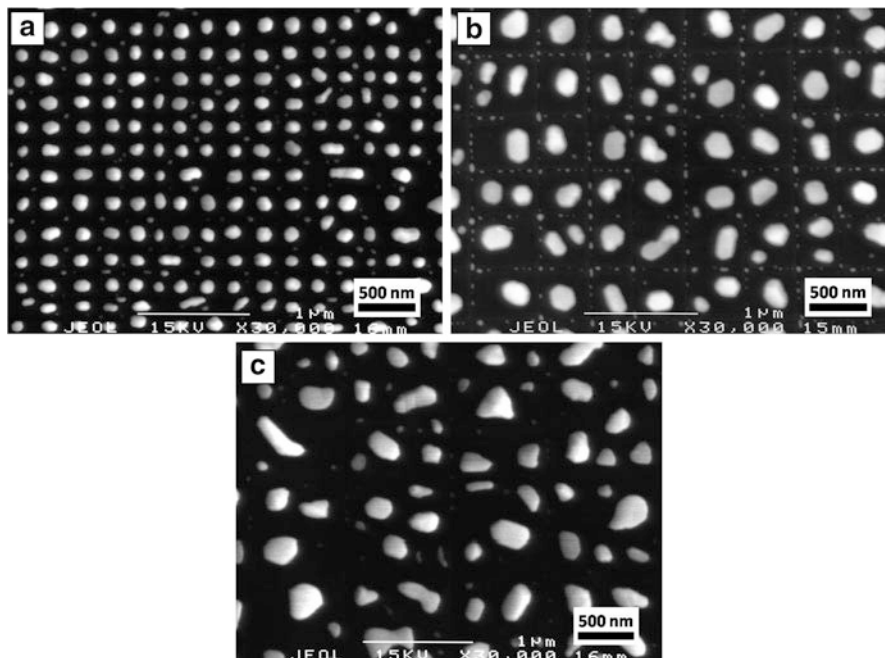
Fig. 24 Nanodot array generated on the patterned substrate. Groove grid size: (**a**) 250 nm, (**b**) 500 nm, and (**c**) 1000 nm

This is because the grid size was too large and film separation occurred in a groove grid.

Figure 25 shows the variation of the average diameter of nanodots (solid symbols) and their standard deviation (open symbols) as a function of the grid size. The average dot diameter does not increase linearly with the grid size. This is because the average dot diameter of the 500 nm grid includes diameters of smaller dots that remained on the grooves. Thus, the relative standard deviation is also large as compared to that of the nanodot array described in the previous section (see Fig. 14). By eliminating the data pertaining to the small dots on the grooves, the average dot diameter for a grid of 500 nm becomes much larger, and the relative standard deviation much smaller. In the case of the 1000 nm grid, the average nanodot diameter becomes equal to approximately 160 nm, which is almost the same as that of the nanodot array described in the previous section (see Fig. 14), and with the random dot pattern in Fig. 4a. Controlling the size using the groove grid was not effective at this experimental condition.

Figure 26 shows FE-SEM micrographs of nanodots agglomerated on the patterned quartz glass substrates after annealing. The groove grid was fabricated by NPF, and the grid size was 100 nm. These substrates were coated with Au films with the thicknesses of 6, 8, 10, 12, 14, and 16 nm. These substrates were then annealed at 600 °C for 10 min. When the gold-coating layer was 6 nm, small randomly
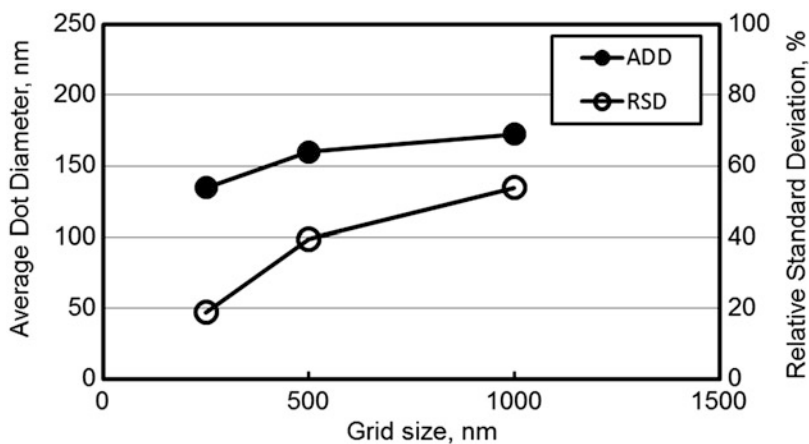
Fig. 25 Variation of the average nanodot size and the relative standard deviation as a function of the grid size
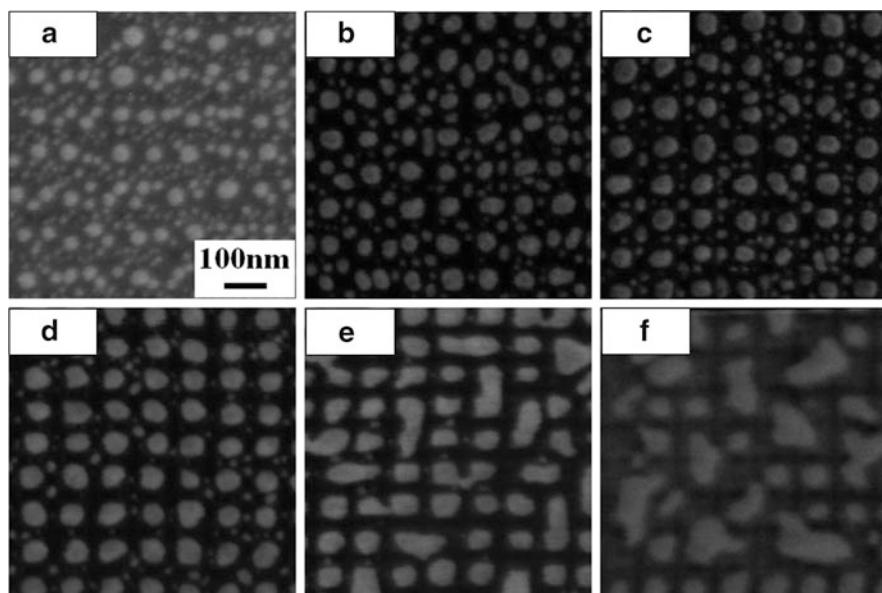
Fig. 26 FE-SEM micrographs of nanodot arrays aggregated on patterned quartz glass substrates after annealing at 600 °C for 10 min. Thickness of the coated film: (**a**) 6 nm, (**b**) 8 nm, (**c**) 10 nm, (**d**) 12 nm, (**e**) 14 nm, and (**f**) 16 nm

distributed dots were generated both on the grid square and on the grooves, and the regularity of the nanodots was poor. When the thickness was 8 nm, the uniformity and regularity of the nanodot array were improved. Some dots aligned approximately at the center of the grid square, but many small dots were located randomly
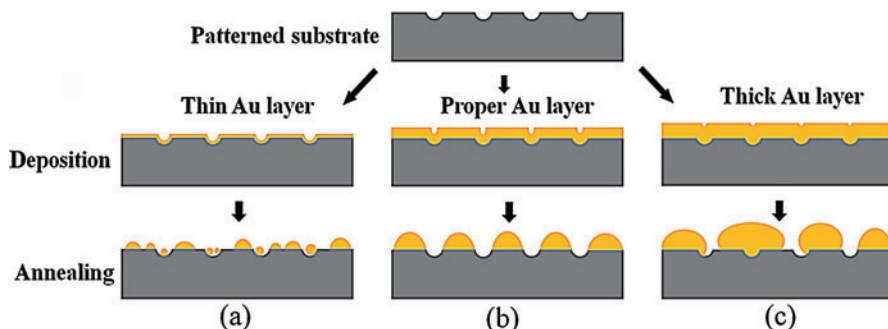
**Fig. 27** Schematic illustration of three types of dot aggregation patterns: (**a**) thin gold film, (**b**) proper gold film thickness, and (**c**) thick gold film

both on the grid square and on the grooves. When the gold film thickness was 10 nm, the uniformity and regularity of the nanodot array were further improved. The dots almost aligned on a grid pattern, and the regularity was apparent. However, only a few small dots remained that were randomly distributed. When the thickness was 12 nm, good nanodot array uniformity and regularity were achieved. The dots aligned at the center of each groove grid. When the thickness was 14 nm, the uniformity and regularity of the nanodot array became worse because some dots were connected to the adjacent dots. When the gold film thickness was 16 nm, the dots were randomly agglomerated on the substrate.

Figure 27 illustrates three types of dot agglomeration patterns observed in the experiments (Truong et al. 2014). When the coated film is very thin, the film is agglomerated into many small dots, as shown in Fig. 27a. These small dots are randomly distributed on the substrate. When the gold film has a proper thickness, as shown in Fig. 27b, the metal film is separated at the grooves, and the metal film on the grid square agglomerates into a dot. As a result, dots of uniform size are aligned in accordance with a grid pattern. When the metal film is too thick, as shown in Fig. 27c, the depth of the grid pattern of the grooves on the gold film surface is too shallow when compared to the thickness of the metal film, and the metal film is not separated at the groove grid perfectly. As a result, some dots are connected with the adjacent dots, and uniformity and regularity of the nanodot array become poor. The control of the thickness of the metal film and the annealing condition is important in order to obtain a nanodot array with good regularity.

Figure 28 shows an example of a grid-patterned substrate and Au nanodots used for a dot transfer experiment. Specifically, Fig. 28a shows an AFM image of the nanogroove grid on the quartz glass substrate. The size of the patterned area of the groove grid was 5×5 mm^2. The grid size was 300 nm, and the width of the groove was 50 nm. Correspondingly, Fig. 28b is the FE-SEM image of the nanodots agglomerated on the substrate using thermal dewetting. The thickness of the coated Au film was 10 nm. The coated substrate was annealed at 800 °C for 10 min. It is found that uniform Au nanodots were agglomerated at the center of each grid square area. These dots were aligned in a lattice pattern, and they formed a nanodot array.
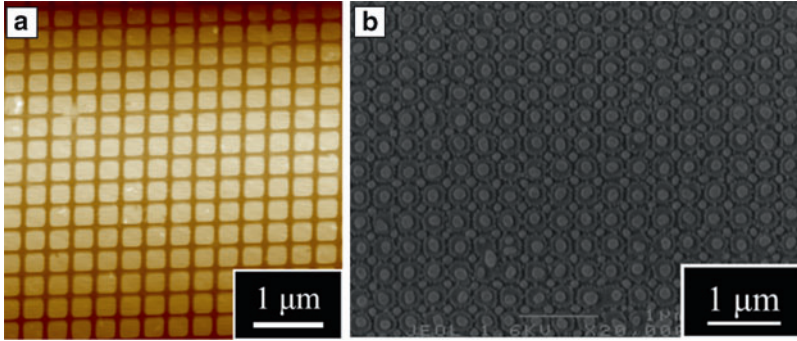
Fig. 28 (**a**) Grid patterned substrate used for dot transfer experiment, and (**b**) Au nanodots generated using coating and annealing

The average dot diameter was approximately 140 nm. Small dots were also agglomerated at the cross points of the grid. These are Au dots that originated at the bottom of the grooves.

Vinyl chloride adhesive was pasted on the Au nanodot array and cured at 50 °C for 30 min to achieve complete dehydration. The cured resin film was then peeled off from the substrate manually. Figure 29 shows an FE-SEM micrograph of (a) the surface of the substrate and (b) the surface of vinyl chloride adhesive after the peeling operation. It was found that most of all the Au nanodots on the substrate were transferred to the adhesive. However, some dots still remained on the substrate, and the dot transfer ratio was not 100%. It is necessary to improve the dot transfer ratio to apply this process to practical industrial production.

4.2   Theoretical Study on the Dot Transfer Mechanism

Figure 30 illustrates two cases that occur in relation to a nanodot in the dot transfer operation:

(a) Case I: a dot is not transferred to the adhesive film but remains on the substrate.
(b) Case II: a dot is transferred to the adhesive film by assuming that the dot shape is semispherical and the shape of the dot does not change through the transfer process.

The total free energy of the system in each case is calculated based on the following equations:

$$W_I = S_s\gamma_s + S_d\gamma_d + S_i\gamma_i + S_s\gamma_p + S_d\gamma_p \quad \text{(case I)} \tag{35}$$
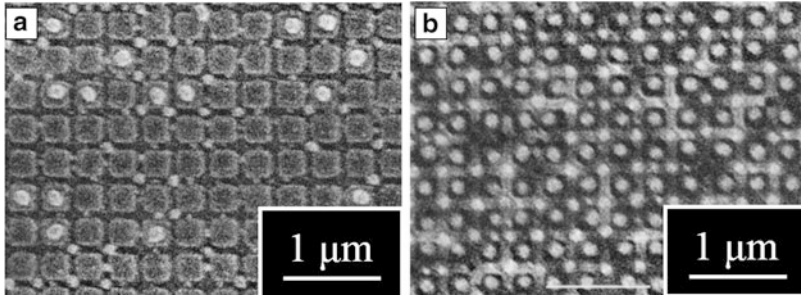
Fig. 29 SEM photographs of surface of (**a**) the substrate and (**b**) vinyl chloride adhesive film after the peeling operation
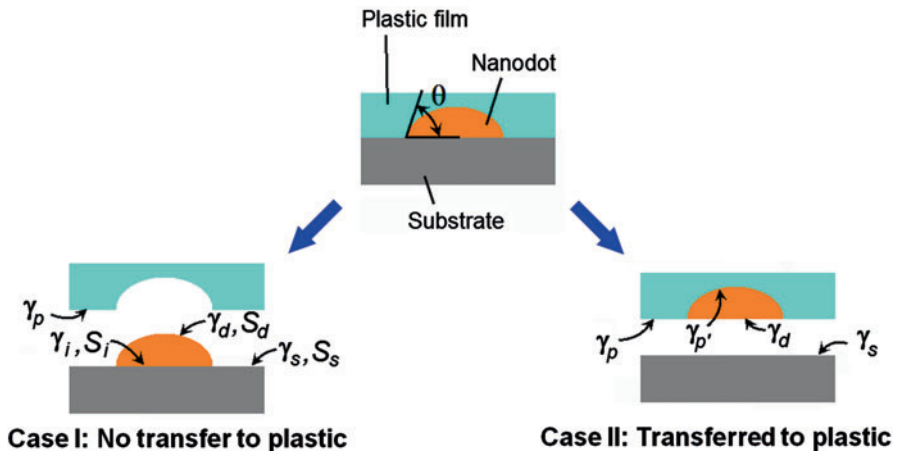
Fig. 30 Model of dot transfer from a substrate to an adhesive film

$$W_{II} = S_s\gamma_s + S_i\gamma_s + S_s\gamma_p + S_i\gamma_d + S_d\gamma_{p'} \quad \text{(case II)} \tag{36}$$

where S_s is the area of substrate surface, S_d is the area of the surface of the dot, and S_i is the interface area between the dot and the substrate. Additionally, γ_s is the surface energy of the substrate, γ_d is the surface energy of the dot, γ_i is the interfacial energy between the dot and the substrate, γ_p is the surface energy of the adhesive, and $\gamma_{p'}$ is the interfacial energy between the dot and the adhesive.

The difference ΔW of the total free energy between cases I and II is calculated as follows:

$$
\begin{aligned}
\Delta W &= W_I - W_{II} \\
&= \left(S_s\gamma_s + S_d\gamma_d + S_i\gamma_i + S_s\gamma_p + S_d\gamma_p\right) - \left(S_s\gamma_s + S_i\gamma_s + S_s\gamma_p + S_i\gamma_d + S_d\gamma_{p'}\right) \\
&= S_d\left(\gamma_d + \gamma_p - \gamma_{p'}\right) + S_i(\gamma_i - \gamma_s - \gamma_d)
\end{aligned}
\tag{37}
$$

Correspondingly, the Young's equation is expressed as follows:

$$\gamma_s - \gamma_i = \gamma_d \cos \theta_c \tag{38}$$

where θ_c is the contact angle between the dot and the substrate. By substituting Eq. 38 into Eq. 37, we obtain

$$\Delta W = S_d(\gamma_d + \gamma_p - \gamma_{p'}) - S_i \gamma_d (1 + \cos \theta_c) \tag{39}$$

The surface area S_d of a dot is calculated using the dot diameter D as follows:

$$S_d = \frac{\pi D^2}{2} \frac{1}{1 + \cos \theta_c} \quad \text{for } \theta_c < 90° \tag{40}$$

$$S_d = \frac{\pi D^2}{2}(1 - \cos \theta_c) \quad \text{for } \theta_c \geq 90° \tag{41}$$

The interfacial area S_i between the dot and the substrate is then calculated as

$$S_i = \frac{\pi D^2}{4} \quad \text{for } \theta_c < 90° \tag{42}$$

$$S_i = \frac{\pi D^2}{4} \sin^2\theta_c \quad \text{for } \theta_c \geq 90° \tag{43}$$

By substituting Eqs. 40, 41, 42, and 43 into Eq. 39, we obtain

$$
\Delta W = W_I - W_{II}
$$
$$
= \begin{cases} \dfrac{\pi D^2}{4} \dfrac{\gamma_d}{1 + \cos \theta_c}\left\{2\left(1 + \dfrac{\gamma_p - \gamma_{p'}}{\gamma_d}\right) - (\cos \theta_c + 1)^2\right\} & \theta_c < 90° \\[3mm] \dfrac{\pi D^2}{4}\gamma_d(1 - \cos \theta_c)\left\{2\left(1 + \dfrac{\gamma_p - \gamma_{p'}}{\gamma_d}\right) - (\cos \theta_c + 1)^2\right\} & \theta_c \geq 90° \end{cases}
\tag{44}
$$

When $\Delta W < 0$, the dot remains on the substrate (case I), while when $\Delta W > 0$, the dot is transferred to the adhesive film (case II).

Figure 31 shows the calculated variation of ΔW as a function of the contact angle θ_c. In this figure, three cases are presented according to balance of surface energies, i.e., $(\gamma_p - \gamma_{p'})/\gamma_d = -1$, 0, and 1, which represent the weak adhesion, intermediate adhesion, and strong adhesion cases, respectively.

It is found from Fig. 31 that ΔW increases as a function of θ_c. In this graph, the three curves represent three levels of adhesion strengths for the adhesive film. The continuous curve represents the adhesive film in the strong adhesion case. In this case, a nanodot is transferred to the film regardless of its contact angle. The dotted curve represents the adhesive in the weak adhesion case. The nanodot is not
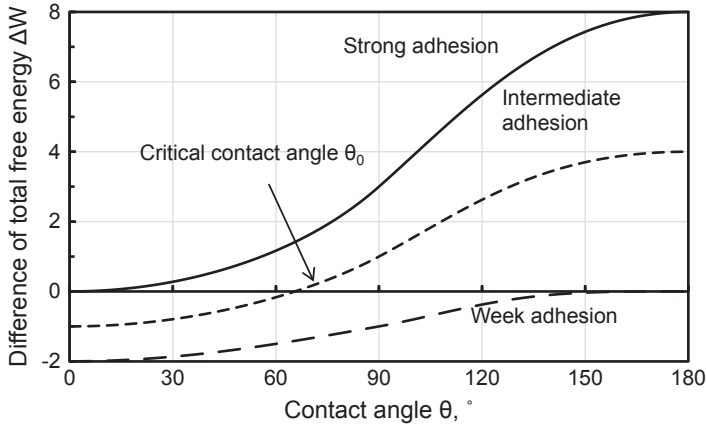
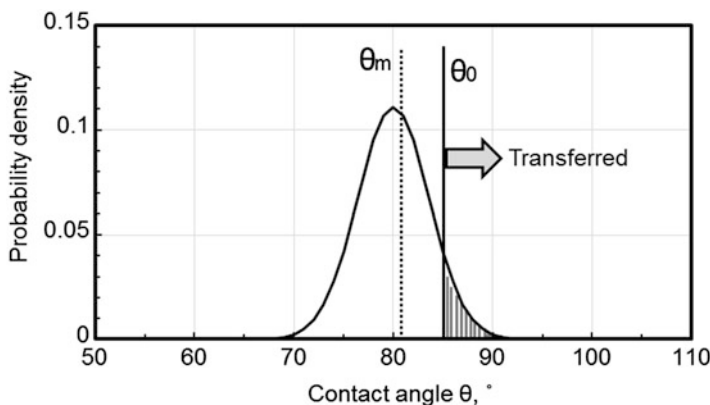**Fig. 31** Variation of ΔW as a function of θ_c

transferred to this plastic regardless of its contact angle. The dashed curve (the center curve) represents the adhesive in the intermediate adhesion case. The nanodot is transferred to the film when the contact angle is large.

In order to calculate the transfer rate, it is necessary to consider variations in the contact angle. Denote the average contact angle as θ_m. The contact angle at which $\Delta W = 0$ is defined as the critical contact angle θ_0. According to the dot transfer theory discussed above, all of the nanodots are transferred when the contact angle θ_c exceeds θ_0, while none of the nanodots are transferred when the contact angle θ is smaller than θ_0. Since there are dispersions in the shapes of the actual nanodots, it is assumed that the contact angle also disperses in accordance with the normal distribution. Assuming that the standard deviation of the contact angle is σ, the probability density function $p(\theta)$ of the contact angle θ is expressed by the following equation:

$$p(\theta) = \frac{1}{\sqrt{2\pi}\sigma} \exp\left\{ -\frac{(\theta - \theta_m)^2}{2\sigma^2} \right\} \tag{45}$$

Figure 32 shows an example of the normal distribution of the contact angles when $\theta_m = 80°$ and $\sigma = 3.6°$. Nanodots whose contact angles are larger than the critical contact angle θ_0 are transferred to the adhesive film. Since the fraction of transferred nanodots is represented by the area highlighted in blue in the graph, the transfer ratio is obtained by dividing this area by total area of the probability density function $p(\theta)$ (=1). Therefore, the transfer ratio T_r is calculated as

$$T_r = \int_{\theta_0}^{\infty} p(\theta) d\theta = \int_{\theta_0}^{\infty} \frac{1}{\sqrt{2\pi}\sigma} \exp\left\{ -\frac{(\theta - \theta_m)^2}{2\sigma^2} \right\} d\theta = \frac{1}{2} + \frac{1}{2}\mathrm{erf}\left(\frac{\theta_m - \theta_0}{\sqrt{2}\sigma} \right) \tag{46}$$

Fig. 32 Normal distribution of contact angles when $\theta_m = 80°$ and $\sigma = 3.6°$

Accordingly, the dot transfer ratio is determined by the error function of the average contact angle θ_m, the critical contact angle θ_0, and the standard deviation σ of the contact angle. Figure 33 shows the variation of the dot transfer ratio as a function of the average contact angle θ_m. The solid line is the theoretical dot transfer ratio calculated by Eq. 46, and the plotted symbols denote the experimental data. The calculated transfer ratio increases smoothly as a function of the average contact angle θ_m. The variation of the theoretical values agrees with the trend of the experimental data. In addition, as the standard deviation σ of the contact angle becomes large, the change of the dot transfer ratio becomes more gradual.

Based on the discussion arguments listed above, it is understood that the dot transfer ratio can be increased by increasing the average contact angle θ_m, and by decreasing the dispersion of the contact angle σ. The adhesion strength $(\gamma_p - \gamma_{p'})/\gamma_d$ of the adhesive film is also factor that affects the dot transfer ratio. The increase of the surface energy of the adhesive, γ_p, and the decrease of the interfacial energy between the dot and the adhesive, $\gamma_{p'}$, increase the dot transfer ratio.

5 Summary and Outlook

A metal nanodot array exhibits unique optical properties. For this reason, it is expected to be used in biosensors and various optical devices. Additionally, a metal nanodot array has a comparably simple structure. As a result, it can be manufactured by conventional lithographic methods. However, the latter involve complicated processes and are associated with high production costs.

In this section, efficient fabrication processes of metal nanodot arrays were introduced using thermal dewetting. The characteristics of the conventional thermal dewetting process were first discussed based on experimental data, and on a physical model of dot agglomeration owing to free energy reduction. A new fabrication process based on grid patterning using NPF and thermal dewetting was then

Fig. 33 Variation of the dot transfer ratio as a function of the average contact angle θ_m
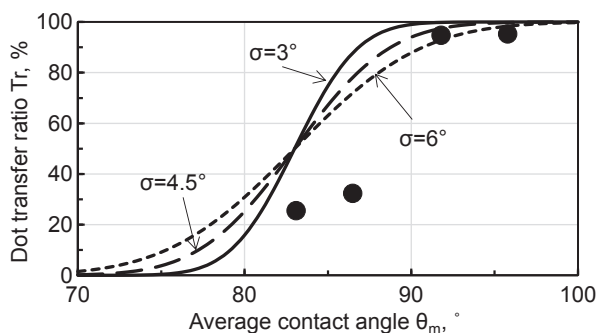
explained. It is useful to manufacture a nanodot array comprising uniform and highly ordered nanodots that could control the dot diameter from several tens to several hundreds of nm. Finally, a manufacturing process was presented for a nanodot array using thermal dewetting on a grid-patterned substrate, and the dot transfer technique was explained. High-throughput production of a nanodot array is expected using this process.

Although there are still many issues that need to be solved, it will be possible to further increase the area size of the nanodot array, increase its productivity, and reduce the production cost in combination with other technologies, such as the nanoimprinting method. It is expected that high-performance sensors and optical devices can be realized using metal nanodot arrays.

References

Agapov RL, Srijanto B, Fowler C, Briggs D, Lavrik NV, Sepaniak MJ (2013). Lithography-free approach to highly efficient, scalable SERS substrates based on disordered clusters of disc-on pillar structures. Nanotechnology 24:505302

Cheung CL, Nikolic RJ, Reinhardt CE, Wang TF (2006). Fabrication of nanopillars by nanosphere lithography. Nanotechnology 17:1339–1343

Cheynis F, Bussmann E, Leroy F, Passanante T, Müller P (2011). Dewetting dynamics of silicon-on-insulator thin films. Phys Rev B 84:245439

Chou SY, Krauss PR, Renstrom PJ (1996). Imprint Lithography with 25-Nanometer Resolution. Science 272:85–87

Danielson DT, Sparacin DK, Michel J, Kimerling LC (2006). Surface-energy-driven dewetting theory of silicon-on-insulator agglomeration. J Appl Phys 100:083507

Dmitriev A, Hägglund C, Chen S, Fredriksson H, Pakizeh T, Käll M, Sutherland DS (2008). Enhanced Nanoplasmonic Optical Sensors with Reduced Substrate Effect. Nano Lett 8:3893–3898

Hong Y, Huh YM, Yoon DS, Yang J (2012). Nanobiosensors Based on Localized Surface Plasmon Resonance for Biomarker Detection. J Nanomater 2012:759830

Huang Z, Meng G, Huang Q, Yang Y, Zhu C, Tang C (2010). Improved SERS Performance from Au Nanopillar Arrays by Abridging the Pillar Tip Spacing by Ag Sputtering. Adv Mater 22:4136–4139

Kajiura M, Nakanishi T, Iida H, Takada H, Osaka T (2009). Biosensing by optical waveguide spectroscopy based on localized surface plasmon resonance of gold nanoparticles used as a probe or as a label. J Colloid Interface Sci 335:140–145

Kandziolka M, Charlton JJ, Kravchenko II, Bradshaw JA, Merkulov IA, Sepaniak MJ, Lavrik NV (2013). Silicon Nanopillars As a Platform for Enhanced Fluorescence Analysis. Anal Chem 85:9031–9038

Knoben W, Brongersma SH, Crego-Calama M (2011). Plasmonic Au islands on polymer nanopillars. Nanotechnology 22:295303

Lee Y, Koh K, Na H, Kim K, Kang JJ, Kim J (2009). Lithography-Free Fabrication of Large Area Subwavelength Antireflection Structures Using Thermally Dewetted Pt/Pd Alloy Etch Mask. Nanoscale Res Lett 4:364–370

Leem JW, Yeh Y, Yu JS (2012). Enhanced transmittance and hydrophilicity of nanostructured glass substrates with antireflective properties using disordered gold nanopatterns. Opt Express 20:4056–4066

Lucas BD, Kim JS, Chin C, Guo LJ (2008). Nanoimprint Lithography Based Approach for the Fabrication of Large-Area, Uniformly-Oriented Plasmonic Arrays†. Adv Mater 20:1129–1134

Mortazavi D, Kouzani AZ, Kaynak A, Duan W (2012). Developing lspr design guidelines. Prog Electromagn Res 126:203–235

Oh YJ, Jeong KH (2012). Glass Nanopillar Arrays with Nanogap-Rich Silver Nanoislands for Highly Intense Surface Enhanced Raman Scattering. Adv Mater 24:2234–2237

Otte MA, Estevez M-C, Carrascosa LG, Gonzalez-Guerrero AB, Lechuga LM, Sepulveda B (2011). Improved Biosensing Capability with Novel Suspended Nanodisks. J Phys Chem C 115:5344–5351

Raphael MP, Christodoulides JA, Mulvaney SM, Miller MM, Long JP, Byers JM (2012). A New Methodology for Quantitative LSPR Biosensing and Imaging. Anal Chem 84:1367–1373

Rayleigh L (1879). On the instability of Jets. Proc Lond Math Soc S1-10(1):4–12

Saito M, Kitamura A, Murahashi M, Yamanaka K, Hoa LQ, Yamaguchi Y, Tamiya E (2012). Novel Gold-Capped Nanopillars Imprinted on a Polymer Film for Highly Sensitive Plasmonic Biosensing. Anal Chem 84:5494–5500

Senanayake P, Hung C-H, Shapiro J, Lin A, Liang B, Williams BS, Huffaker DL (2011). Surface Plasmon-Enhanced Nanopillar Photodetectors. Nano Lett 11:5279–5283

Sepulveda B, Angelome PC, Lechuga LM, Liz-Marzan LM (2009). LSPR-based nanobiosensors. NanoToday 4:244–251

Tan CL, Jang SJ, Lee YT (2012). Localized surface plasmon resonance with broadband ultralow reflectivity from metal nanoparticles on glass and silicon subwavelength structures. Opt Express 20:17448–17455

Truong DP, Yamanaka A, Yoshino M (2012). High Throughput Method to Fabricate Ordered Nano Dot Array on Various Plastic Films. Key Eng Mater 523–524:633–638

Truong DP, Terano M, Yoshino M (2014). Fabrication of an ordered nanodot array by thermal dewetting on a patterned substrate. Manuf Lett 2(2):60–63. https://doi.org/10.1016/j.mfglet.2014.02.004

Tsai SJ, Ballarotto M, Romero DB, Herman WN, Kan HC, Phaneuf RJ (2010). Effect of gold nanopillar arrays on the absorption spectrum of a bulk heterojunction organic solar cell. Opt Express 18:A528–A535

Varghese LT, Fan L, Xuan Y, Tansarawiput C, Kim S, Qi M (2013). Resistless Nanoimprinting in Metal for Plasmonic Nanostructures. Small 9:3778–3783

Yoshino M, Ohsawa H, Yamanaka A (2011). Rapid fabrication of an ordered nano-dot array by the combination of nano-plastic forming and annealing methods. J Micromech Microeng 21:125017

Yoshino M, Osawa H, Yamanaka A (2012). Effects of process conditions on nano-dot array formation by thermal dewetting. J Manuf Process 14:478–486

Yoshino M, Li Z, Terano M (2015). Theoretical and Experimental Study of Metallic Dot Agglomeration Induced by Thermal Dewetting. J Micro Nano-Manuf 3(2):021004

Young T (1805). An essay on the cohesion of fluids. Phil Trans R Soc London 95:65–87

Zeng S, Yong K, Roy I, Dinh X, Yu X, Luan F (2011). A Review on Functionalized Gold Nanoparticles for Biosensing Applications. Plasmonics 6(3):491–506. https://doi.org/10.1007/s11468-011-9228-1

Zhang W, Ding F, Li WD, Wang Y, Hu J, Chou SY (2012). Giant and uniform fluorescence enhancement over large areas using plasmonic nanodots in 3D resonant cavity nanoantenna by nanoimprinting. Nanotechnology 23:225301

Zhigal'skii GP, Jones BK (2003) Taylor & Francis, London. The physical properties of thin metal films. Chap. 4, ISBN:0-415-28390-6